Crystal field magnetostriction of spin ice under ultrahigh magnetic fields

Nan Tang, Masaki Gen, Martin Rotter, Huiyuan Man, Kazuyuki Matsuhira, Akira Matsuo, Koichi Kindo, Akihiko Ikeda, Yasuhiro H. Matsuda, Philipp Gegenwart, Satoru Nakatsuji, Yoshimitsu Kohama

Angaben zur Veröffentlichung / Publication details:

Tang, Nan, Masaki Gen, Martin Rotter, Huiyuan Man, Kazuyuki Matsuhira, Akira Matsuo, Koichi Kindo, et al. 2024. "Crystal field magnetostriction of spin ice under ultrahigh magnetic fields." Physical Review B 110 (21): 214414. https://doi.org/10.1103/physrevb.110.214414.

Crystal field magnetostriction of spin ice under ultrahigh magnetic fields

Nan Tang [1,*,†] Masaki Gen [2,*,‡] Martin Rotter [3] Huiyuan Man [4] Kazuyuki Matsuhira [5] Akira Matsuo,[2] Koichi Kindo,[2] Akihiko Ikeda [2,6] Yasuhiro H. Matsuda [2] Philipp Gegenwart [1] Satoru Nakatsuji [2,7,8,9] and Yoshimitsu Kohama [2]

[1]*Experimental Physics VI, Center for Electronic Correlations and Magnetism, University of Augsburg, 86159 Augsburg, Germany*
[2]*Institute for Solid State Physics, University of Tokyo, Kashiwa, Chiba 277-8581, Japan*
[3]*McPhase Project, 01159 Dresden, Germany*
[4]*Geballe Laboratory for Advanced Materials, Stanford University, California 94305, USA*
[5]*Faculty of Engineering, Kyushu Institute of Technology, Kitakyushu, Fukuoka 804-8550, Japan*
[6]*Department of Engineering Science, University of Electro-Communications, Chofu, Tokyo 182-8585, Japan*
[7]*Department of Physics, University of Tokyo, Tokyo 113-0033, Japan*
[8]*Institute for Quantum Matter and Department of Physics and Astronomy, Johns Hopkins University, Baltimore, Maryland 21218, USA*
[9]*Trans-scale Quantum Science Institute, University of Tokyo, Tokyo 113-0033, Japan*

(Received 7 September 2024; revised 29 October 2024; accepted 1 November 2024; published 9 December 2024)

We present a comprehensive study of the magnetoelastic properties of the Ising pyrochlore oxide $Ho_2Ti_2O_7$, known as spin ice, by means of high-field magnetostriction measurements and numerical calculations. When a magnetic field is applied along the crystallographic ⟨111⟩ axis, the longitudinal magnetostriction exhibits a broad maximum in the low-field regime around 30 T, followed by a dramatic lattice contraction due to crystal-field (CF) level crossing at $B_{cf} \sim 65$ T. The transverse magnetostriction exhibits a contrasting behavior, highlighting the anisotropic nature of the CF striction. By applying a magnetic field at varying sweep rates, we identify distinct timescales of spin dynamics that are relevant to monopole formation and annihilation, as well as CF-phonon dynamics. Our mean-field calculations, based on a point-charge model, successfully reproduce the overall magnetostriction behavior, revealing the competition between the exchange striction and CF striction. A signature of the CF level crossing is also observed through adiabatic magnetocaloric-effect measurements, consistent with our magnetostriction data.

DOI: 10.1103/PhysRevB.110.214414

I. INTRODUCTION

Magnetostriction refers to the distortion of a lattice when a material is subjected to an external magnetic field. Certain magnetostrictive materials exhibit relative length change $\Delta L/L$ as large as several percent [1,2]. These materials have been extensively studied for their practical applications in developing multifunctional devices, such as actuators, oscillators, and sensors [3,4]. Beyond their applicative aspects, magnetostriction serves as a key physical quantity for probing phase transitions as well as underlying spin correlations. For instance, magnetostriction measurements on the quantum spin ice $Pr_2Zr_2O_7$ revealed a sharp first-order transition at extremely low temperatures, shedding light on a liquid-gas metamagnetic transition and offering insights into spin-orbital liquids [5,6]. Magnetostriction measurements on the Shastry-Sutherland magnet $SrCu_2(BO_3)_2$ uncovered a series of spin superstructure phases under ultrahigh magnetic fields [7,8], which are characterized by devil's-staircase-like magnetization plateaus [9].

There are several well-known microscopic origins of magnetostriction [10]. One such mechanism involves the dependence of an ionic radius on its electronic configuration. A field-induced change in the ionic state can result in significant volume magnetostriction, as exemplified by a spin-state transition in $LaCoO_3$ [11] and valence transitions in f electron-based valence-fluctuating materials [12–14]. In contrast to these on-site mechanisms, exchange striction refers to the change in distance between two magnetic ions to minimize exchange coupling energy [Fig. 1(a)]. Here, $\Delta L/L$ reflects changes in local spin correlations $\langle \boldsymbol{S}_i \cdot \boldsymbol{S}_j \rangle$ between neighboring sites i and j, and consequently correlates with the magnetization M [7,15–17]. The crystal field (CF) also influences the arrangement of surrounding anions and the wavefunction of the magnetic site to minimize Coulomb energy. Applying a magnetic field alters the wavefunction through CF level hybridization, potentially causing anisotropic lattice deformation, known as CF striction [Fig. 1(b)]. Although magnetostriction is universally observed in all magnetic materials, its theoretical description is far from straightforward and is often simplified by phenomenological approaches [18] or effective magnetoelastic models [19,20].

The target compound in this study is $Ho_2Ti_2O_7$, one of the most extensively studied $4f$ Ising pyrochlore magnet, known as a classical spin ice [21–33]. The strong Ising

*These authors contributed equally to this work.
†Contact author: nan.tang@uni-a.de
‡Contact author: gen@issp.u-tokyo.ac.jp

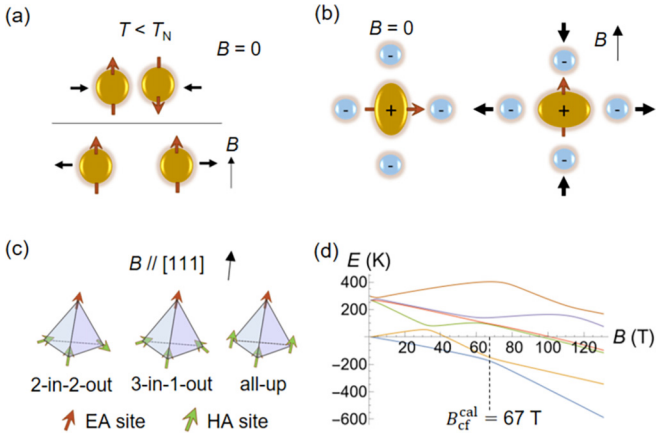

FIG. 1. (a), (b) Schematics of (a) exchange striction and (b) crystal-field (CF) striction. The orange arrows indicate the magnetic moments, and the yellow (blue) spheres represent the valence electron density of the magnetic ion (ligands). The elliptical deformation of the yellow spheres schematically illustrates the crystal-field anisotropy, which aligns with the magnetic moment direction. The thick black arrows indicate the direction of ion displacement when the magnetic moment orientation is altered by an external magnetic field B. (c) Three types of spin configurations when a magnetic field is applied along [111] on $Ho_2Ti_2O_7$. The spins aligned along the easy axis are colored orange (EA site), while those aligned along the hard axis are colored green (HA site). (d) Energy level diagram for the single-ion Hamiltonian of Eq. (2), where one of the three HA spins is subjected to a magnetic field in the [111] direction. The two lowest CF levels hybridize at $B_{\rm cf}^{\rm cal} = 67$ T.

anisotropy along the ⟨111⟩ axes arises from a combination of dominant nearest-neighbor ferromagnetic interactions and the CF effects. This leads to a highly degenerate ground state characterized by short-range spin correlations, where two spins point inward and two point outward within each tetrahedron ("2-in-2-out") [25] [Fig. 1(c)]. When a magnetic field is applied along the [111] direction, a metamagnetic transition occurs at approximately 2 T, flipping one spin and resulting in a "3-in-1-out" (or "1-in-3-out") configuration in the tetrahedra, representing a fully polarized state within the Ising limit [Fig. 1(c)]. In this field orientation, each tetrahedron has one magnetic site with the easy axis parallel to B [the easy-axis (EA) site] and three sites with axes not parallel to B [the hard-axis (HA) sites].

Given the strong spin-orbit coupling that links spin and orbital degrees of freedom, the CF-phonon interaction plays a key role in magnetoelastic properties, forming the foundation of magnetostrictive phenomena. However, as the easy-axis directions vary at the four magnetic sites in $Ho_2Ti_2O_7$, local lattice deformations induced by the CF tend to cancel out, making its effect on the crystal structure less evident. To clarify this, the observation of the CF striction in high magnetic fields would be useful. In $Ho_2Ti_2O_7$, the energy gap between the lowest and the first-excited CF levels is approximately 260 K in zero field [22,31]. The application of an external magnetic field along [111] can hybridize these CF levels at the HA sites, as shown in the CF level diagram in Fig. 1(d), eventually realizing a forced ferromagnetic (all-up) state [Fig. 1(c)]. The CF level crossing is theoretically expected at $B_{\rm cf}^{\rm cal} = 67$ T based on the exact diagonalization of the CF Hamiltonian. Indeed, Erfanifam *et al.* observed a signature of the CF level hybridization for $B \parallel [111]$ through magnetization and ultrasound measurements up to 60 T [29], and Opherden *et al.* observed a sequence of metamagnetic transitions accompanied by the CF level crossing for $B \parallel [5513]$ up to 120 T [32].

Here, we investigate the CF striction in $Ho_2Ti_2O_7$ using magnetostriction measurements under ultrahigh magnetic fields up to 120 T, complemented by magnetization and magnetocaloric effect (MCE) measurements. We observe significant anisotropic CF striction, characterized by a lattice contraction amounting to $\Delta L/L \sim -5 \times 10^{-4}$ along the field direction. We were also able to resolve the timescale of spin dynamics, finding it to be comparable to the microsecond range, relevant to monopole formation and annihilation. Additionally, CF-phonon dynamics appear to occur at rates that are comparable to, or potentially even faster than, the microsecond range. Our mean-field calculations, based on a point-charge model and incorporating CF, two-ion exchange interactions, phonons, and CF-phonon coupling, successfully reproduce the magnetostriction data. Similar high-field magnetostriction is observed in another spin-ice compound, $Pr_2Zr_2O_7$, suggesting that the CF striction is a common feature in rare-earth-based spin-ice systems.

II. METHODS

A. Experiments

Single crystals of $Ho_2Ti_2O_7$ and $Pr_2Zr_2O_7$ were grown from polycrystalline feed rods using a high-temperature xenon-type optical floating zone furnace at ISSP, University of Tokyo. Crystal orientations were checked using a backscattering Laue x-ray diffractometer. Several pieces of as-grown crystals were cut and polished into rectangular parallelepipeds with dimensions of approximately $1 \times 1 \times 3$ mm^3.

We performed magnetization and magnetostriction measurements in the field orientation $B \parallel [111]$. Magnetization up to 7 T was measured using a superconducting quantum interference device (MPMS, Quantum Design). Magnetization up to 62 T and 130 T was measured by the induction method in a nondestructive short-pulsed magnet (4 ms duration) and in a horizontal single-turn-coil (HSTC) system (8 μs duration) [34], respectively. Longitudinal magnetostriction ($\Delta L/L \parallel [111]$) up to 55 T and 118 T was measured by the fiber-Bragg-grating (FBG) method in a nondestructive long-pulsed magnet (36 ms duration) and in the HSTC system, respectively. Transverse magnetostriction ($\Delta L/L \perp [111]$) up to 55 T was also measured in the nondestructive long-pulsed magnet, where the optical fiber was bent by 90 degrees, as in Refs. [14,35]. A relative sample-length change $\Delta L/L$ was detected by the optical filter method [36]. The optical fiber was glued on the flat surface of the crystal using Stycast1266.

In the nondestructive pulsed magnet, the magnetization and magnetostriction measurements were performed in either liquid-^{4}He or gas ^{4}He environment, i.e., nonadiabatic conditions. In the HSTC system, the sample was cooled to approximately 5 K using a liquid-^{4}He flow-type cryostat, where the measurement condition should be quasiadiabatic because

TABLE I. Experimental conditions for magnetization M, magnetostriction $\Delta L/L$, and magnetocaloric effect (MCE) measurements.

	Pulsed magnet	Field duration	Maximum field	Temperature conditions
M	HSTC	8 μs	130 T	Quasiadiabatic
	Nondestructive short pulse	4 ms	62 T	Nonadiabatic
$\Delta L/L$	HSTC	8 μs	120 T	Quasiadiabatic
	Nondestructive long pulse	36 ms	55 T	Nonadiabatic
MCE	Nondestructive long pulse	36 ms	55 T	Quasiadiabatic & nonadiabatic

of the short pulsed-field duration. To monitor the temperature change of the sample during the field sweep, we measured the magnetocaloric effect (MCE) up to 55 T under both nonadiabatic and quasiadiabatic conditions using the nondestructive long-pulsed magnet [37]. A sensitive $Au_{16}Ge_{84}$ film thermometer was sputtered on the surface of the crystal, with temperature calibration performed using a commercial RuO_2 thermometer.

Table I summarizes the measurement conditions for all experiments conducted under pulsed magnetic fields. The typical magnetic-field profiles of the three types of magnets used in the experiments are shown in Fig. 7 in Appendix A.

B. Theoretical calculations

To capture the CF level scheme in $Ho_2Ti_2O_7$, we first consider a single-ion Hamiltonian that includes both the CF and Zeeman terms. The CF Hamiltonian can be expressed as follows:

$$\hat{H}_{\rm cf} = \sum_{lm} B_{lm} O_{lm} \tag{1}$$

where B_{lm} denotes the CF parameters, and O_{lm} represents Stevens operator equivalents. The single-ion Hamiltonian is then written as

$$\hat{H}_{\text{single-ion}} = \hat{H}_{\rm cf} - g_J \mu_{\rm B} \hat{\boldsymbol{J}}_i \cdot \boldsymbol{B}, \tag{2}$$

where g_J is the Landé's g factor, $\mu_{\rm B}$ is the Bohr magneton, $\hat{\boldsymbol{J}}_i$ is the magnetic moment at site i, and $\boldsymbol{B}$ is the external magnetic field. We obtain the field evolution of the CF level energy at the HA site [Fig. 1(d)] by exact diagonalization of Eq. (2) [38].

For detailed analyses of magnetization and magnetostriction, we additionally take into account magnetic interactions, phonons, and CF-phonon coupling. The magnetic properties of $Ho_2Ti_2O_7$ can be accurately described by the classical dipolar spin-ice model, incorporating dominant long-range dipolar interaction $J_{\rm dipo}$ and short-range nearest-neighbor exchange interaction $J_{\rm ex}$. As the dipolar interaction $J_{\rm dipo}$ can be effectively renormalized into the nearest-neighbor exchange interaction [24], we consider a two-spin exchange coupling term described by

$$\hat{H}_{\rm ex} = -\frac{1}{2}\sum_{ij} J(\boldsymbol{R}_{ij}) \hat{\boldsymbol{J}}_i \hat{\boldsymbol{J}}_j, \tag{3}$$

where the sum is taken over all nearest-neighbor pairs, $J(\boldsymbol{R}_{ij}) \equiv J_{\rm dipo} + J_{\rm ex}$ is the distance-dependent effective exchange coupling, and $\boldsymbol{R}_{ij}$ is the vector connecting sites i and j. Assuming that J is linearly modulated by a small strain ϵ, we expand $J(\boldsymbol{R}_{ij})$ as,

$$J(\boldsymbol{R}_{ij}) \approx J\left(\boldsymbol{R}^0_{ij}\right) + \sum_{\alpha,\gamma=1,2,3,\beta=1,\ldots,6} \frac{\partial J}{\partial R^\alpha} \frac{\partial \epsilon_{\alpha\gamma} R^\gamma_{ij}}{\partial \epsilon_\beta} \epsilon_\beta, \tag{4}$$

where $\boldsymbol{R}^0_{ij}$ is the distance between the original positions of sites i and j, and the indices $\alpha, \gamma = x, y, z$ refer to an Euclidean coordinate system parallel to the crystal axes, i.e., $x \parallel a$, $y \parallel b$ and $z \parallel c$. The index β follows Voigt notation, ranging from 1–6. In other words, ϵ_β represents the strain tensor $\epsilon_{\alpha\gamma}$ in Voigt notation. For the lattice contribution, we consider a phonon term, $\hat{H}_{\rm ph}$, and a CF-phonon term, $\hat{H}_{\rm cfph}$, which represents the coupling between the CF and phonons. The detailed formulas for these two terms are provided in Appendix B. Combining all these terms, we construct the total Hamiltonian as

$$\hat{H}_{\rm total} = \sum_i \hat{H}_{\text{single-ion}} + \hat{H}_{\rm ex} + \hat{H}_{\rm ph} + \hat{H}_{\rm cfph}. \tag{5}$$

We performed numerical simulations based on Eq. (5) using the MCPHASE program [39–41], which specializes in calculating the physical properties of $4f$-based magnets within the framework of mean-field theory [42–44]. MCPHASE employs a point-charge model to determine the CF wave functions and CF energy gap [38]. To match the experimental energy gap of approximately 260 K [22,31], we apply a scaling factor of 0.7 to the nominal charges Ho (3+), Ti (4+), O (2−). To set the initial state in zero field, we utilized the crystallographic parameters of $Ho_2Ti_2O_7$ reported in Ref. [45]. We set the dipolar interaction to $J_{\rm dipo} = 2.4$ K [24] and the nearest-neighbor exchange interaction to $J_{\rm ex} = 0.1$ K, yielding a total effective exchange coupling of $J = 2.5$ K. This set of parameters successfully reproduces both the metamagnetic transition in the low-field regime and the CF level crossing at $B_{\rm cf} \sim 65$ T, as experimentally observed. We note that even a small change of 0.1 K in $J_{\rm ex}$ results in a 6 T shift in $B^{\rm cal}_{\rm cf}$. In Eq. (4), we assume $dJ/dR \simeq dJ_{\rm ex}/dR$, which is determined by the Bethe-Slater curve, as shown in Fig. 8 in Appendix B.

To calculate the magnetization, we solve the mean-field equations self-consistently to obtain the magnetization at each sublattice i, which is given by

$$\boldsymbol{M}_i = \sum_n \frac{g_J \mu_{\rm B} \langle n|\hat{\boldsymbol{J}}_i|n\rangle}{Z} \exp(-E_n/k_{\rm B}T), \tag{6}$$

where $Z = \sum_n \exp(-E_n/k_{\rm B}T)$ is the partition function for sublattice i, and $|n\rangle$ is the eigenstate corresponding to the eigenvalue E_n of $\hat{H}_{\rm total}$ treated in mean-field approximation.

The total magnetization M is obtained by averaging the magnetization of all sublattices, in the unit of μ_B/Ho.

For the magnetostriction, we calculate strains self-consistently using Eq. (5) and the following equation:

$$\sum_{\beta=1,\ldots,6} c^{\alpha\beta}\epsilon_\beta = \sum_{i,\delta=1,2,3} G^{\alpha\delta}_{\rm mix}(i)\langle u_i^\delta\rangle + \sum_{i,lm} G^{\alpha lm}_{\rm cfph}(i)\langle O_{lm}(\hat{\boldsymbol{J}}_i)\rangle + \frac{1}{2}\sum_{i,i',\delta,\delta',\alpha',\gamma=1,2,3} \frac{\partial J_{\delta\delta'}(\boldsymbol{R}_{ii'})}{\partial R^{\alpha'}} \frac{\partial \epsilon_{\alpha'\gamma}\partial R^\gamma_{ii'}}{\partial \epsilon_\alpha} \times \langle \hat{J}_{i\delta}\hat{J}_{i'\delta'}\rangle, \quad (7)$$

where i, i', δ, δ', α', and γ run over the spatial coordinates x, y, and z, represented as the integers 1, 2, and 3, respectively. $c^{\alpha\beta}$ denotes the elastic constant, where α and β are indices in Voigt notation, ranging from 1–6. $G^{\alpha\delta}_{\rm mix}$ represents the phonon-strain coupling, and $G^{\alpha lm}_{\rm cfph}$ represents the CF-phonon coupling. For details of these parameters, see Appendix B. In Eq. (7), the first and second terms on the right side contribute to the CF striction, and the third term is the exchange striction. The total lattice strain, i.e., magnetostriction, can be obtained by

$$\frac{\Delta L}{L} = \sum_{i,j=1,2,3} \epsilon_{ij}\boldsymbol{l}_i\boldsymbol{l}_j, \quad (8)$$

where $\boldsymbol{l}$ denotes the unit vector in the direction of measurement. Strain ϵ_{ij} is a 3×3 symmetric tensor, hence has six independent matrix elements: ϵ_{xx}, ϵ_{yy}, ϵ_{zz}, ϵ_{xy}, ϵ_{xz}, ϵ_{yz}. We obtain the longitudinal magnetostriction ($\Delta L/L \parallel [111]$) by calculating $\Delta L/L = (\epsilon_{xx}+\epsilon_{yy}+\epsilon_{zz}+2(\epsilon_{xy}+\epsilon_{xz}+\epsilon_{yz}))/3$. In this study, we use Voigt notation, where ϵ_{ij} is relabeled as $\epsilon_1=\epsilon_{xx}$, $\epsilon_2=\epsilon_{yy}$, $\epsilon_3=\epsilon_{zz}$, $\epsilon_4=2\epsilon_{yz}=2\epsilon_{zy}$, $\epsilon_5=2\epsilon_{xz}=2\epsilon_{zx}$, and $\epsilon_6=2\epsilon_{xy}=2\epsilon_{yx}$.

III. RESULTS AND DISCUSSION

A. High-field magnetization and magnetostriction

Figure 2(a) shows the magnetization curve of $Ho_2Ti_2O_7$ for $B \parallel [111]$ measured up to 130 T at an initial temperature of $T_{\rm ini} = 5$ K using the HSTC system. The M–B curve measured up to 62 T at $T_{\rm ini} = 4.2$ K using the nondestructive pulsed magnet is also displayed, which reproduces Ref. [29]. Both M–B curves exhibit a plateaulike feature between 20 and 60 T, followed by a metamagnetic increase, where the field derivative of magnetization dM/dB exhibits a broad peak at $B_{\rm cf} \sim$ 65 T for the field-down sweep [see the inset of Fig. 2(a)]. This metamagnetic behavior suggests the CF level crossing at the HA sites, consistent with the CF scheme shown in Fig. 1(d). Above $B_{\rm cf}$, M gradually approaches the expected full moment, 10 μ_B/Ho, suggesting the realization of the all-up state. We note that the sensitivity of magnetization detection decreases as dB/dt approaches zero, which may introduce errors in the absolute value of M near the maximum field.

Figure 2(b) shows the longitudinal magnetostriction curve for $B \parallel [111]$ measured up to 120 T at $T_{\rm ini} = 5$ K using the HSTC system, along with the curve measured up to 55 T at $T_{\rm ini} = 4.2$ K using the nondestructive pulsed magnet. Initially, $\Delta L/L$ increases and reaches a maximum around 30 T. Subsequently, $\Delta L/L$ reverses and dramatically decreases from 30–80 T, where the field derivative of the magnetostriction

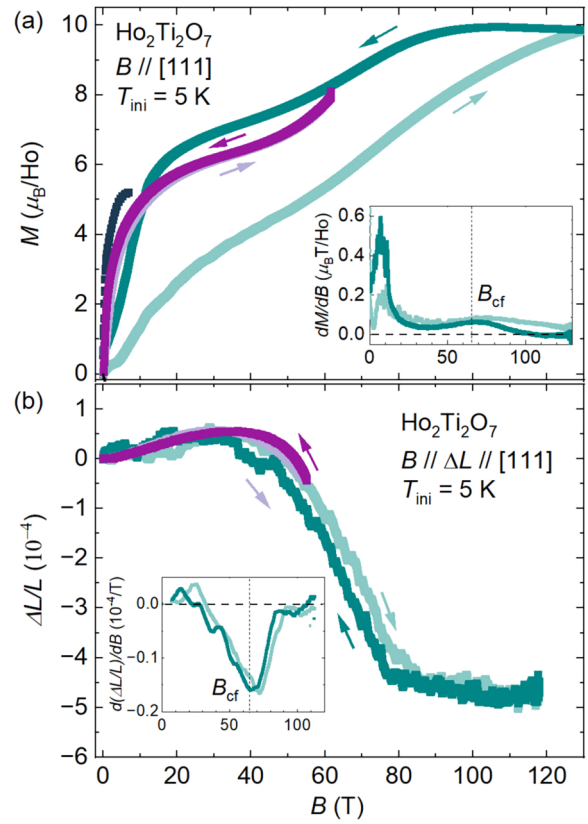

FIG. 2. Magnetic-field dependence of (a) magnetization M and (b) longitudinal magnetostriction $\Delta L/L \parallel [111]$ in $Ho_2Ti_2O_7$ for $B \parallel [111]$ in ultrahigh magnetic fields. Black symbols in (a) show the M–B data measured at $T = 4.2$ K using the MPMS, purple symbols show the data measured at $T_{\rm ini} = 4.2$ K using the nondestructive pulsed magnet, and green symbols show the data measured at $T_{\rm ini} = 5$ K using the HSTC system. The insets of (a) and (b) show the field derivatives of magnetization dM/dB and magnetostriction $d(\Delta L/L)/dB$, respectively, for the HSTC data. The critical field of the CF level crossing $B_{\rm cf}$ is defined using the field-down sweep data.

$d(\Delta L/L)/dB$ exhibits a peak at $B_{\rm cf} \sim$ 65 T for the field-down sweep [see the inset of Fig. 2(b)]. Finally, $\Delta L/L$ is nearly saturated at ~80 T. The observed change in sample length across $B_{\rm cf}$, amounting to $\Delta L/L \sim 5\times10^{-4}$, highlights the strong CF effect on the crystal structure of $Ho_2Ti_2O_7$.

B. Magnetocaloric effect (MCE)

Comparing the three M–B curves shown in Fig. 2(a), it is evident that the initial rise in magnetization at low magnetic fields becomes more gradual as the field sweep becomes faster. This trend could be attributed to two factors: sample heating and slow spin relaxation. We will discuss the spin dynamics in Sec. III C. To verify the sample heating, we performed MCE measurements for $B \parallel [111]$ up to 55 T in the nondestructive pulsed magnet. The field dependence of the sample temperature $T(B)$, measured at various initial temperatures ($T_{\rm ini}$'s) under quasiadiabatic conditions, are shown by the blue curves in Fig. 3. The $T(B)$ curves for field-up and field-down sweeps overlap for all the measured $T_{\rm ini}$'s. The absence of hysteresis ensures that nearly adiabatic conditions

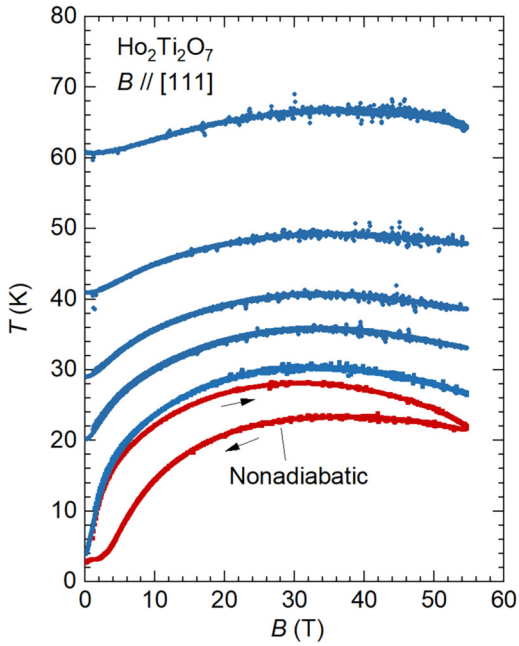

FIG. 3. Magnetocaloric effect in $Ho_2Ti_2O_7$ for $B \parallel [111]$ measured at various T_{ini}'s under quasiadiabatic conditions (blue), and at $T_{ini} = 4.2$ K under nonadiabatic conditions (red).

were achieved. These $T(B)$ curves can hence be regarded as isentropic, meaning that the total entropy, comprising both lattice entropy and magnetic entropy, remains constant.

For $T_{ini} = 5$ K, $T(B)$ approaches 30 K at 30 T, indicating a significant reduction in magnetic entropy [46]. This occurs because the highly degenerate 2-in-2-out states are destroyed by a magnetic field as weak as 2 T, stabilizing the nondegenerate 3(1)-in-1(3)-out state. At higher initial temperatures, the increase in $T(B)$ is less pronounced due to greater thermal fluctuations and larger lattice heat capacity. After $T(B)$ reaches its maximum around 35 T, the sample gradually cools as the magnetic field increases up to 55 T. This cooling behavior indicates an increase in magnetic entropy, suggesting the onset of CF level hybridization.

We also measured the sample temperature changes at $T_{ini} = 4.2$ K in a liquid-^{4}He environment, i.e., under nonadiabatic conditions, as shown by the red curve in Fig. 3. Surprisingly, $T(B)$ reaches 28 K during the field-up sweep, which is only slightly lower than in the quasiadiabatic case. These MCE results indicate that sample heating effects are unavoidable when measuring $Ho_2Ti_2O_7$ in pulsed high magnetic fields. We infer that, in the magnetization and magnetostriction data presented in Fig. 2, the sample temperature is likely between 20 and 30 K at fields above 10 T.

C. Spin dynamics

Our high-field data also provide valuable insights into the dynamic properties of the magnetic state. In the experimental data obtained using the millisecond-duration pulsed magnetic fields [Figs. 7(a) and 7(b)], both the M–B curve up to 62 T and the $\Delta L/L$–B curve up to 55 T exhibit small hysteresis (Fig. 2). The hysteresis is likely caused by a lower sample temperature during the field-down sweep compared to the field-up sweep, as suggested by our nonadiabatic MCE data (Fig. 3). We note that the hysteresis loop in the $\Delta L/L - B$ curve cannot be attributed to slow spin dynamics because the sign of the hysteresis is opposite to what would be expected from a delayed response. Therefore, the small hysteresis observed in millisecond-duration pulsed magnetic-fields suggests the timescale of spin relaxation is faster than the millisecond range, which will be discussed in more detail in the next paragraph.

In contrast, the M–B curve up to 130 T, obtained in the microsecond-duration pulsed magnetic fields [Fig. 7(c)] under quasiadiabatic condition, exhibits significant hysteresis [Fig. 2(a)]. Given that no hysteresis is observed in the quasiadiabatic MCE (Fig. 3), the observed hysteresis can be attributed to slow spin relaxation, which mainly originates from nonequilibrium processes of monopole formation or annihilation [44]. Together with the magnetization data from millisecond-pulsed fields, the spin dynamics appears to be faster than the millisecond but slower than or comparable to the microsecond regime, consistent with previous studies based on neutron spin echo and ac susceptibility experiments [47]. However, inelastic neutron scattering experiments have reported a different timescale of 10 ns, suggesting the presence of faster processes [48]. The reason for such discrepancy has been addressed in Ref. [49].

Notably, the hysteresis observed in the $\Delta L/L$–B curve up to 120 T is much less pronounced compared to that in the M–B curve (Fig. 2), a difference that cannot be explained by temperature effects, as both experiments were performed under quasiadiabatic condition. The overall sample-length change of $Ho_2Ti_2O_7$ in high magnetic fields primarily originates from CF striction, with a smaller contribution from exchange striction (see Sec. III E), making CF striction the main source of hysteresis. This suggests that the dynamics of CF-striction is likely within or faster than the microsecond range. It is important to note that potential contributions from slower spin-lattice dynamics cannot be excluded, given the absence, to the best of our knowledge, of previous research on such interactions in $Ho_2Ti_2O_7$, as these dynamics should occur beyond the timescale of our pulsed-field experiments. Further investigation into the dynamics of spin-lattice interactions in $Ho_2Ti_2O_7$ would be valuable for future work.

D. Temperature dependence and anisotropic magnetostriction

We also investigate the anisotropy and temperature dependence of the magnetostriction. Figures 4(a) and 4(b) show the longitudinal and transverse magnetostriction of $Ho_2Ti_2O_7$, respectively, for $B \parallel [111]$ measured at various T_{ini}'s in the nondestructive pulsed magnet. As T_{ini} increases, the position of the hump in the longitudinal magnetostriction curve shifts to a lower field, and eventually, the hump disappears at $T_{ini} = 60$ K.

In contrast to the longitudinal magnetostriction, the transverse magnetostriction at $T_{ini} = 4.2$ K exhibits a broad dip around 30 T. As the temperature increases to $T_{ini} = 40$ K, this dip structure disappears, and $\Delta L/L$ begins to increase steadily with the magnetic field. The anisotropic behavior between the longitudinal and transverse magnetostricition at high magnetic fields is the characteristic of the CF striction.

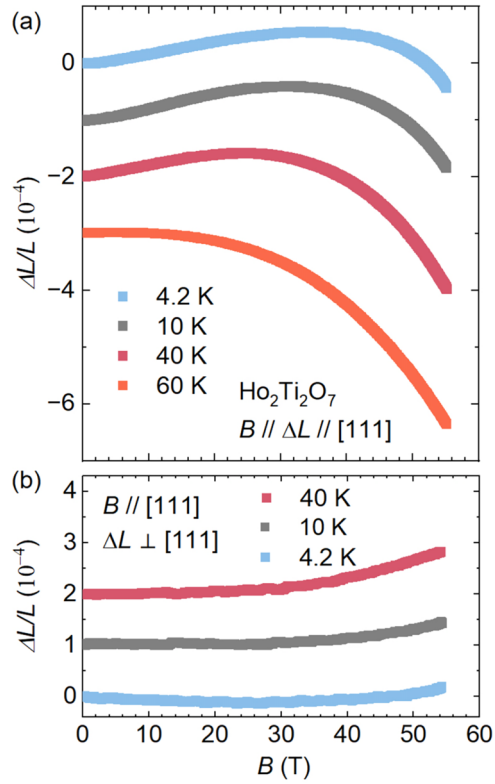

FIG. 4. Temperature dependence of (a) longitudinal and (b) transverse magnetostriction in $Ho_2Ti_2O_7$ for $B \parallel [111]$. The data except for $T_{ini} = 4.2$ K are offset for clarity.

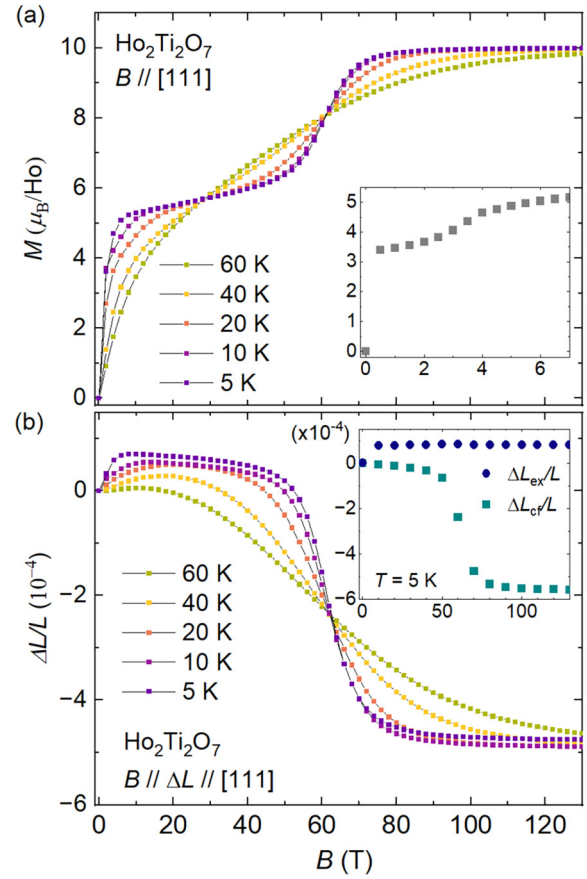

FIG. 5. Calculation results of (a) M–B curves and (b) $\Delta L/L$–B curves for the Hamiltonian in Eq. (5), obtained by mean-field approach. The inset of (a) shows an enlarged view of the M–B curve at 5 K in the low-field regime, clarifying a metamagnetic behavior from the 2-in-2-out to the 3(1)-in-1(3)-out state. In the inset of (b), the circle and square symbols represent the contributions from exchange striction ($\Delta L_{ex}/L$) and crystal-field (CF) striction ($\Delta L_{cf}/L$), respectively, to the total magnetostriction at 5 K.

E. Numerical calculations

To theoretically understand the behavior of M and $\Delta L/L$ in high magnetic fields, we performed numerical calculations based on the mean-field approach for the Hamiltonian in Eq. (5). Figures 5(a) and 5(b) show the calculated M–B and $\Delta L/L$–B curves, respectively, for $B \parallel [111]$ at various temperatures. By adopting the 2-in-2-out spin-ice structure as the initial state in zero field, the metamagnetic transition to the 3(1)-in-1(3)-out state is reproduced at 5 K, as shown in the inset of Fig. 5(a). At low temperatures below 20 K, a plateaulike feature appears between 10 and 50 T, followed by another metamagnetic transition at approximately 65 T induced by the CF level crossing. These trends are qualitatively consistent with the experimentally observed M–B curve [Fig. 2(a)]. The less pronounced plateaulike feature and broader metamagnetic behavior in the experimental curve can be attributed to the MCE and slow spin relaxation, as mentioned in Secs. III B and III C.

Having confirmed that our simulations accurately describe the magnetization of $Ho_2Ti_2O_7$ across the entire field range, we now turn to the longitudinal magnetostriction. According to Eq. (7), the total magnetostriction is composed of the CF striction ($\Delta L_{cf}/L$) and exchange striction ($\Delta L_{ex}/L$). The field dependence of $\Delta L_{cf}/L$ and $\Delta L_{ex}/L$ at 5 K is plotted in the inset of Fig. 5(b), where $\Delta L_{cf}/L$ becomes more prominent in the high-field regime. The combination of a positive change in $\Delta L_{ex}/L$ in the low-field regime and a negative change in $\Delta L_{cf}/L$ in the high-field regime results in a hump structure centering around 30 T in the total magnetostriction curve. Notably, the rounded shape of the experimentally observed hump in the $\Delta L/L$–B curve at $T_{ini} = 5$ K [Fig. 2(b)] is presumably due to sample heating, which is consistent with the calculated $\Delta L/L$–B curve at 20 K. Our calculations predict that the hump in $\Delta L/L$ shifts to a lower magnetic field with increasing temperature and eventually disappears above 60 K. This behavior also agrees well with the experimental observations, as shown in Fig. 4(a).

F. Prevalence of CF striction in spin-ice compounds

We have revealed the CF striction in $Ho_2Ti_2O_7$ through both experimental and theoretical approaches. Applying a magnetic field along the [111] direction leads to the hybridization of the lowest and first-excited CF levels around B_{cf}, which is associated with negative longitudinal magnetostriction and positive transverse magnetostriction. To explore whether the CF striction is a common feature of spin-ice systems, we investigated high-field magnetostriction in another spin-ice compound, $Pr_2Zr_2O_7$. The introduction of rare-earth ions with

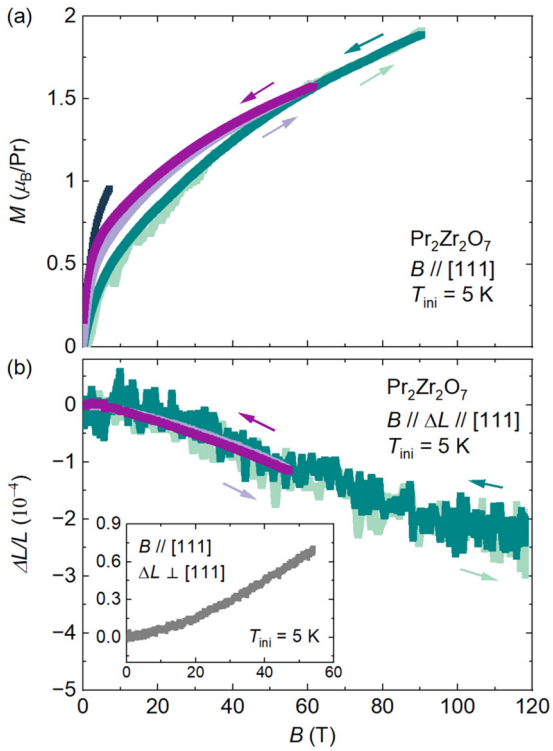

FIG. 6. Magnetic-field dependence of (a) magnetization M and (b) longitudinal magnetostriction $\Delta L/L \parallel [111]$ in $Pr_2Zr_2O_7$ for $B \parallel [111]$ in ultrahigh magnetic fields. Black symbols in (a) show the M–B data measured at $T = 4.2$ K using the MPMS, purple symbols show the data measured at $T_{ini} = 4.2$ K using the nondestructive pulsed magnet, and green symbols show the data measured at $T_{ini} = 5$ K using the HSTC system. The inset of (b) shows the transverse magnetostriction data measured at $T_{ini} = 4.2$ K using the nondestructive pulsed magnet.

smaller magnetic moments, such as Pr ($\sim$3 μ_B), can modify the spin-ice state, making it less Ising-like and more susceptible to quantum effects. In particular, $Pr_2(Zr, Sn, Hf, Ir)_2O_7$ are proposed as quantum spin ices [6,50–54]. The lowest CF level of $Pr_2Zr_2O_7$ consists of 90–96% of $|J = \pm 4\rangle$ [52,53] (smaller compared to 98% of $|J = \pm 8\rangle$ in $Ho_2Ti_2O_7$), indicating the presence of substantial transverse fluctuations.

Figures 6(a) and 6(b) display the M–B and $\Delta L/L$–B curves for $Pr_2Zr_2O_7$ at $T_{ini} = 5$ K (or 4.2 K), respectively. No hysteresis is observed, consistent with the reported fast spin dynamics on the picosecond timescale [52]. Unlike $Ho_2Ti_2O_7$, the magnetization shows a monotonic increase without any plateaulike features, suggesting that $Pr_2Zr_2O_7$ does not exhibit a well-defined Ising limit state, and the low-energy CF levels gradually hybridize as the magnetic field increases.

Notably, the longitudinal magnetostriction in $Pr_2Zr_2O_7$ decreases monotonically, while the transverse magnetostriction increases. This anisotropic lattice deformation is similar to that observed in $Ho_2Ti_2O_7$ (Fig. 4), suggesting that the similar CF environments in $Ho_2Ti_2O_7$ and $Pr_2Zr_2O_7$ lead to qualitatively identical CF striction effects. We note that the sign of the magnetostriction in the low-field regime for $Pr_2Zr_2O_7$ is opposite to that for $Ho_2Ti_2O_7$. This difference is likely due to the opposite signs of dJ/dR for $Ho_2Ti_2O_7$ ($dJ/dR > 0$) and $Pr_2Zr_2O_7$ ($dJ/dR < 0$).

IV. CONCLUSION

We have thoroughly investigated the static and dynamic magnetoelastic properties in the spin-ice compound $Ho_2Ti_2O_7$ through magnetostriction measurements under ultrahigh magnetic fields. Our observations reveal a large anisotropic magnetostriction occurring at the CF level crossing around $B_{cf} \sim 65$ T, where the longitudinal magnetostriction amounts to $\Delta L/L \sim -5 \times 10^{-4}$. Complementary MCE measurements reveal a dramatic sample-heating effect exceeding 20 K in pulsed high-field experiments, and also highlight the onset of CF level hybridization above 30 T, which would correlate with the turnaround behavior of the magnetostriction curve. By varying the magnetic field sweep rates, we distinguish between the fast dynamics of the CF-phonon coupling and the slower dynamics of spin-spin correlations, associated with monopole creation and annihilation.

To model the CF striction, we developed a comprehensive Hamiltonian based on a point-charge model that includes CF-phonon coupling. Our numerical calculations based on a mean-field approach successfully reproduce the experimental magnetostriction data across the entire field range, showing a dominant contribution from CF striction $\Delta L/L_{cf}$ and a much smaller contribution from exchange striction $\Delta L/L_{ex}$. This study paves the way for understanding the intricate role of the CF-phonon coupling in the crystal structure of a broad range of $4f$-based magnets.

ACKNOWLEDGMENTS

This work was partly supported by the Deutsche Forschungsgemeinschaft (DFG, German Research Foundation) via TRR 360 (Project No. 492547816), JSPS KAKENHI Grants-In-Aid for Scientific Research (Grants No. 20J10988 and No. 24H01633), JST-ASPIRE Program (JPMJAP2317), and JST-MIRAI Program (JPMJMI20A1). N.T. was supported by the Alexander von Humboldt foundation. M.G. was supported by the JSPS through a Grant-in-Aid for JSPS Fellows. We gratefully acknowledge the enduring support of T. Sakakibara and the stimulating discussions with R. Moessner, R. Klingeler, M. Gingras, T. Fennell, and M. Udagawa.

APPENDIX A: WAVEFORM OF PULSED HIGH MAGNETIC FIELDS

Figure 7 shows the typical magnetic-field profiles generated by three types of pulsed magnets used in this study.

APPENDIX B: PHONON AND CF-PHONON COUPLING TERMS

In this section, we provide the formulas for the phonon term $\hat{H}_{ph}$ and the CF-phonon coupling term $\hat{H}_{cfph}$ in the Hamiltonian of Eq. (5). $\hat{H}_{ph}$ is written as follows:

$$\hat{H}_{ph} = \sum_i \frac{\boldsymbol{p}_i^2}{2m_i} + \frac{1}{2}\sum_{ij} \frac{k_{ij}}{2|R_{ij}|^2}(\boldsymbol{U}_j\boldsymbol{R}_{ij} - \boldsymbol{U}_i\boldsymbol{R}_{ij})^2. \quad \text{(B1)}$$

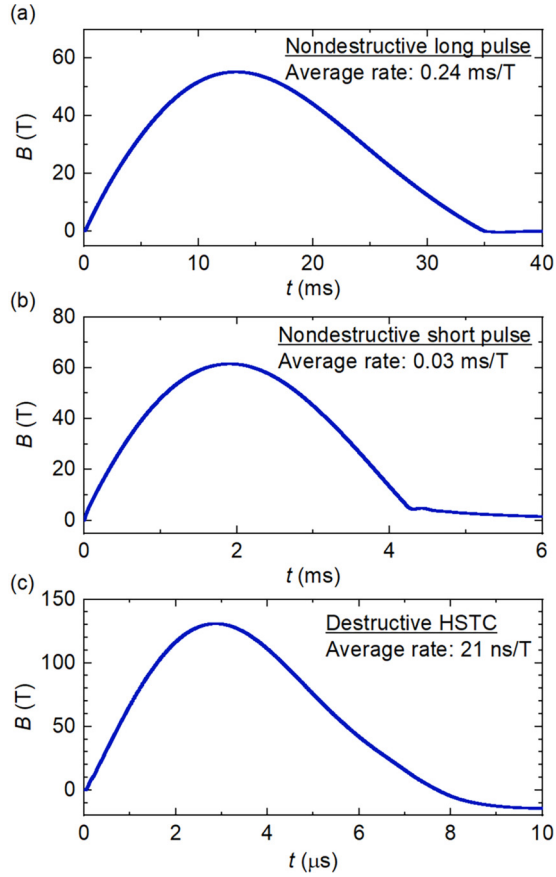

FIG. 7. Typical waveform of the generated pulsed magnetic field in (a) the nondestructive long pulsed magnet, (b) the nondestructive short pulsed magnet, and (c) the horizontal single-turn-coil (HSTC) system. The averaged field-sweep rates for the field-up sweep are 240 μs/T, 30 μs/T, and 21 ns/T, respectively.

Here, $\boldsymbol{p}_i$ and m_i denote the momentum and mass, respectively, of the atom at position i. The displacement vector of the atom at position i is represented by $\boldsymbol{U}_i$. The difference between the undisplaced lattice positions is given by $\boldsymbol{R}_{ij} \equiv \boldsymbol{R}_j - \boldsymbol{R}_i$, where $\boldsymbol{R}_j$ ($\boldsymbol{R}_i$) represents the position of atom at site j (i). k_{ij} is the longitudinal atomic spring constants, which is determined based on the Born-von Karman model, assuming simple distance-dependence (see Appendix C for details). The spring constants are then used to define the phonon-strain coupling constant G_{mix} as follows:

$$G^{\alpha\beta\gamma}_{\text{mix}}(i) = -\,a_0 \sum_i \frac{k_{ij}}{|\boldsymbol{R}_{ij}|^2} \boldsymbol{R}^{\alpha}_{ij} \boldsymbol{R}^{\beta}_{ij} \boldsymbol{R}^{\gamma}_{ij}, \tag{B2}$$

where a_0 is the Bohr radius, and the indices $\alpha, \beta, \gamma = x, y, z$ refer to an Euclidean coordinate system parallel to the crystal axes, i.e., $x \parallel a$, $y \parallel b$ and $z \parallel c$. To be noted, in Eq. (7), α and β are used in Voigt notation ($\alpha, \beta = 1, \ldots, 6$), and are defined differently than in this context.

The CF-phonon coupling is expressed by

$$\hat{H}_{\text{cfph}} = \sum_{lm} \sum_{ij(i<j)} \nabla_{\boldsymbol{U}_i} B_{lm}(j) \boldsymbol{U}_i O_{lm}(\hat{\boldsymbol{J}}_j), \tag{B3}$$

where the index i denotes all atomic positions, B_{lm} denotes the CF parameters, and O_{lm} represents Stevens operator

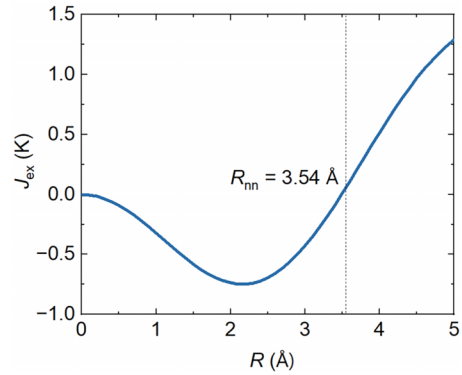

FIG. 8. Distance dependence of the nearest-neighbor exchange interaction J_{ex}, as described by the Bethe-Slater curve. The nearest-neighbour distance is $R_{\text{nn}} = 3.54$ Å [45].

equivalents. The CF-phonon coupling constant G_{cfph} can be derived from Eq. (B3) by taking the displacement derivative of the CF parameters as

$$G^{\alpha\beta lm}_{\text{cfph}}(j) = -\frac{1}{2} \sum_i \left(R^{\beta}_i \frac{\partial B_{lm}(j)}{\partial \boldsymbol{U}^{\alpha}_i} + R^{\alpha}_i \frac{\partial B_{lm}(j)}{\partial \boldsymbol{U}^{\beta}_i} \right). \tag{B4}$$

Again, in Eq. (7), α and β are used in Voigt notation ($\alpha, \beta = 1, \ldots, 6$), and are defined differently than in this context. Importantly, G_{cfph} affects the magnitude of $\Delta L/L$. We scaled G_{cfph} obtained from MCPHASE by a factor of 0.16 to match the calculated $\Delta L/L$ with the experimental one. Although the elastic constants $c^{\alpha\beta}$ also affect the magnitude of $\Delta L/L$, their values were fixed based on prior experimental data, as detailed in Appendix C.

In order to obtain the positional derivative of the exchange interaction J_{ex}, the Bethe-Slater curve is employed, as shown in Fig. 8:

$$J_{\text{ex}}(R) = A[-(R/D)^2 + (R/D)^4] \exp^{-(R/D)^2}, \tag{B5}$$

where A and D are set to 0.4 and 3.49, respectively, resulting in $J_{\text{ex}} = 0.1$ K and $dJ_{\text{ex}}/dr = 1.03$ K/Å at the nearest-neighbor distance $R_{\text{nn}} = 3.54$ Å [45]. It is important to constrain dJ_{ex}/dr to a positive value for $Ho_2Ti_2O_7$ in order to explain the positive longitudinal magnetostriction in the low-field regime.

APPENDIX C: ELASTIC CONSTANTS

MCPHASE computes the spring constants k_{ij} in units of N/m based on the Born-von Karman model:

$$k_{ij} = k_0 \times \exp(-gr^2), \quad k_0 = 800\ \text{N/m}, \quad g = 0.1\ \text{Å}^{-2}, \tag{C1}$$

where i, j denotes spatial directions x, y, z, k_0 and g are adjustable fitting coefficients used to obtain the appropriate elastic constants, and r is bond length in the unit of Å. Springs for neighbours up to a distance of 7.5 Å are taken into account. Based on these spring constants, the elastic constant tensor $c^{\alpha\beta}$ can be derived. The resulting tensor closely matches those obtained from sound velocity experiments [27] and successfully reproduces both the slope of low-energy acoustic phonons as a function of wave vectors and the highest-energy optical phonon mode, which reaches

105 meV in DFT calculations [30]. Equation (C1) produces a table of longitudinal spring constants, which are then converted to an elastic tensor with three independent elements in the units of eV/primitive unit cell: $c_{11} = 585.656$, $c_{12} = 276.629$, and $c_{44} = 276.629$, reflecting the highly symmetric cubic crystal structure. These values are in good agreement with those obtained from ultrasound measurements [27], after performing a unit conversion of 1 meV/primitive unit cell volume = 0.000621 GPa, where the primitive unit cell volume is 257.835 Å^3 [45].

[1] K. B. Hathaway and A. E. Clark, Magnetostrictive materials, MRS Bull. **18**, 34 (1993).

[2] Q. Yu, J. Wang, C. Liang, J. Meng, J. Xu, Y. Liu, S. Zhao, X. Xi, C. Xi, M. Yang, C. Si, Y. He, D. Wang, and C. Jiang, A giant magneto-superelasticity of 5% enabled by introducing ordered dislocations in $Ni_{34}Co_8Cu_8Mn_{36}Ga_{14}$ single crystal, Adv. Sci. **11**, 2401234 (2024).

[3] H. Zhang, T. Zhang, and C. Jiang, Magnetostrictive actuators with large displacement and fast respons, Smart Mater. Struct. **21**, 055014 (2012).

[4] V. Apicella, C. S. Clemente, D. Davino, D. Leone, and C. Visone, Review of modeling and control of magnetostrictive actuators, Actuators **8**, 45 (2019).

[5] A. S. Patri, M. Hosoi, S. B. Lee, and Y. B. Kim, Theory of magnetostriction for multipolar quantum spin ice in pyrochlore materials, Phys. Rev. Res. **2**, 033015 (2020).

[6] N. Tang, Y. Gritsenko, K. Kimura, S. Bhattacharjee, A. Sakai, M. Fu, H. Takeda, H. Man, K. Sugawara, Y. Matsumoto, Y. Shimura, J. Wen, C. Broholm, H. Sawa, M. Takigawa, T. Sakakibara, S. Zherlitsyn, J. Wosnitza, R. Moessner, and S. Nakatsuji, Spin–orbital liquid state and liquid–gas metamagnetic transition on a pyrochlore lattice, Nat. Phys. **19**, 92 (2023).

[7] M. Jaime, R. Daou, S. A. Crooker, F. Weickert, A. Uchida, A. E. Feiguin, C. D. Batista, H. A. Dabkowska, and B. D. Gaulin, Magnetostriction and magnetic texture to 100.75 Tesla in frustrated $SrCu_2(BO_3)_2$, Proc. Natl. Acad. Sci. USA **109**, 12404 (2012).

[8] T. Nomura, P. Corboz, A. Miyata, S. Zherlitsyn, Y. Ishii, Y. Kohama, Y. H. Matsuda, A. Ikeda, C. Zhong, H. Kageyama, and F. Mila, Unveiling new quantum phases in the Shastry-Sutherland compound $SrCu_2(BO_3)_2$ up to the saturation magnetic field, Nat. Commun. **14**, 3769 (2023).

[9] Y. H. Matsuda, N. Abe, S. Takeyama, H. Kageyama, P. Corboz, A. Honecker, S. R. Manmana, G. R. Foltin, K. P. Schmidt, and F. Mila, Magnetization of $SrCu_2(BO_3)_2$ in ultrahigh magnetic fields up to 118 T, Phys. Rev. Lett. **111**, 137204 (2013).

[10] M. Doerr, M. Rotter, and A. Lindbaum, Magnetostriction in rare-earth based antiferromagnets, Adv. Phys. **54**, 1 (2005).

[11] A. Ikeda, Y. H. Matsuda, and K. Sato, Two spin-state crystallizations in $LaCoO_3$, Phys. Rev. Lett. **125**, 177202 (2020).

[12] K. Yoshimura, T. Nitta, M. Mekata, T. Shimizu, T. Sakakibara, T. Goto, and G. Kido, Anomalous high-field magnetization and negative forced volume magnetostriction in $Yb_{1-x}M_xCu_2$ (M=In and Ag)–evidence for valence change in high magnetic fields, Phys. Rev. Lett. **60**, 851 (1988).

[13] N. V. Mushnikov and T. Goto, High-field magnetostriction of the valence-fluctuating compound $YbInCu_4$, Phys. Rev. B **70**, 054411 (2004).

[14] A. Miyake, M. Gen, A. Ikeda, K. Miyake, Y. Shimizu, Y. J. Sato, D. Li, A. Nakamura, Y. Homma, F. Honda, J. Flouquet, M. Tokunaga, and D. Aoki, Magnetovolume effect on the first-order metamagnetic Transition in UTe_2, J. Phys. Soc. Jpn. **91**, 063703 (2022).

[15] V. S. Zapf, V. F. Correa, P. Sengupta, C. D. Batista, M. Tsukamoto, N. Kawashima, P. Egan, C. Pantea, A. Migliori, J. B. Betts, M. Jaime, and A. Paduan-Filho, Direct measurement of spin correlations using magnetostriction, Phys. Rev. B **77**, 020404(R) (2008).

[16] A. Ikeda, S. Furukawa, O. Janson, Y. H. Matsuda, S. Takeyama, T. Yajima, Z. Hiroi, H. Ishikawa, Magnetoelastic couplings in the deformed kagome quantum spin lattice of volborthite, Phys. Rev. B **99**, 140412(R) (2019).

[17] A. Miyata, T. Hikihara, S. Furukawa, R. K. Kremer, S. Zherlitsyn, and J. Wosnitza, Magnetoelastic study on the frustrated quasi-one-dimensional spin-$\frac{1}{2}$ magnet $LiCuVO_4$, Phys. Rev. B **103**, 014411 (2021).

[18] A. S. Patri, A. Sakai, S. B. Lee, A. Paramekanti, S. Nakatsuji, and Y. B. Kim, Unveiling hidden multipolar orders with magnetostriction, Nat. Commun. **10**, 4092 (2019).

[19] S. Kimura, M. Hagiwara, T. Takeuchi, H. Yamaguchi, H. Ueda, and K. Kindo, Exchange interactions of the chromium spinel oxide $HgCr_2O_4$ in high magnetic fields examined by the magnetoelastic theory, J. Phys. Soc. Jpn. **83**, 113709 (2014).

[20] A. Miyata, H. Suwa, T. Nomura, L. Prodan, V. Felea, Y. Skourski, J. Deisenhofer, H. A. Krug von Nidda, O. Portugall, S. Zherlitsyn, V. Tsurkan, J. Wosnitza, and A. Loidl, Spin-lattice coupling in a ferrimagnetic spinel: Exotic H–T phase diagram of $MnCr_2S_4$ up to 110 T, Phys. Rev. B **101**, 054432 (2020).

[21] M. J. Harris, S. T. Bramwell, D. F. McMorrow, T. Zeiske, and K. W. Godfrey, Geometrical frustration in the ferromagnetic pyrochlore $Ho_2Ti_2O_7$, Phys. Rev. Lett. **79**, 2554 (1997).

[22] S. Rosenkranz, A. P. Ramirez, A. Hayashi, R. J. Cava, R. Siddharthan, and B. S. Shastry, Crystal-field interaction in the pyrochlore magnet $Ho_2Ti_2O_7$, J. Appl. Phys. **87**, 5914 (2000).

[23] K. Matsuhira, Y. Hinatsu, K. Tenya, and T. Sakakibara, Low temperature magnetic properties of frustrated pyrochlore ferromagnets $Ho_2Sn_2O_7$ and $Ho_2Ti_2O_7$, J. Phys.: Condens. Matter **12**, L649 (2000).

[24] S. T. Bramwell and M. J. P. Gingras, Spin ice state in frustrated magnetic pyrochlore materials, Science **294**, 1495 (2001).

[25] O. A. Petrenko, M. R. Lees, and G. Balakrishnan, Magnetization process in the spin-ice compound $Ho_2Ti_2O_7$, Phys. Rev. B **68**, 012406 (2003).

[26] T. Fennell, P. P. Deen, A. R. Wildes, K. Schmalzl, D. Prabhakaran, A. T. Boothroyd, R. J. Aldus, D. F. McMorrow, and S. T. Bramwell, Magnetic coulomb phase in the spin ice $Ho_2Ti_2O_7$, Science **326**, 415 (2009).

[27] Y. Nakanishi, T. Kumagai, M. Yoshizawa, K. Matsuhira, S. Takagi, and Z. Hiroi, Elastic properties of the rare-earth dititanates $R_2Ti_2O_7$ (R = Tb, Dy, and Ho), Phys. Rev. B **83**, 184434 (2011).

[28] C. Castelnovo, R. Moessner, and S. L. Sondhi, Spin ice, fractionalization, and topological order, Annu. Rev. Condens. Matter Phys. **3**, 35 (2012).

[29] S. Erfanifam, S. Zherlitsyn, S. Yasin, Y. Skourski, J. Wosnitza, A. A. Zvyagin, P. McClarty, R. Moessner, G. Balakrishnan, and O. A. Petrenko, Ultrasonic investigations of the spin ices $Dy_2Ti_2O_7$ and $Ho_2Ti_2O_7$ in and out of equilibrium, Phys. Rev. B **90**, 064409 (2014).

[30] M. Ruminy, M. N. Valdez, B. Wehinger, A. Bosak, D. T. Adroja, U. Stuhr, K. Iida, K. Kamazawa, E. Pomjakushina, D. Prabakharan, M. K. Haas, L. Bovo, D. Sheptyakov, A. Cervellino, R. J. Cava, M. Kenzelmann, N. A. Spaldin, and T. Fennell, First-principles calculation and experimental investigation of lattice dynamics in the rare-earth pyrochlores $R_2Ti_2O_7$ ($R =$ Tb, Dy, Ho), Phys. Rev. B **93**, 214308 (2016).

[31] M. Ruminy, E. Pomjakushina, K. Iida, K. Kamazawa, D. T. Adroja, U. Stuhr, and T. Fennell, Crystal-field parameters of the rare-earth pyrochlores $R_2Ti_2O_7$ ($R =$ Tb, Dy, and Ho), Phys. Rev. B **94**, 024430 (2016).

[32] L. Opherden, T. Herrmannsdörfer, M. Uhlarz, D. I. Gorbunov, A. Miyata, O. Portugall, I. Ishii, T. Suzuki, H. Kaneko, H. Suzuki, and J. Wosnitza, Magnetization beyond the Ising limit of $Ho_2Ti_2O_7$, Phys. Rev. B **99**, 085132 (2019).

[33] Y. Wang, T. Reeder, Y. Karaki, J. Kindervater, T. Halloran, N. Maliszewskyj, Y. Qiu, J. A. Rodriguez, S. Gladchenko, S. M. Koohpayeh, S. Nakatsuji, and C. Broholm, Monopolar and dipolar relaxation in spin ice $Ho_2Ti_2O_7$, Sci. Adv. **7**, eabg0908 (2021).

[34] M. Gen, Y. Okamoto, M. Mori, K. Takenaka, and Y. Kohama, Magnetization process of the breathing pyrochlore magnet $CuInCr_4S_8$ in ultrahigh magnetic fields up to 150 T, Phys. Rev. B **101**, 054434 (2020).

[35] M. Gen, A. Miyake, H. Yagiuchi, Y. Watanabe, A. Ikeda, Y. H. Matsuda, M. Tokunaga, T. Arima, and Y. Tokunaga, Enhancement of giant magnetoelectric effect in Ni-doped $CaBaCo_4O_7$, Phys. Rev. B **105**, 214412 (2022).

[36] A. Ikeda, T. Nomura, Y. H. Matsuda, S. Tani, Y. Kobayashi, H. Watanabe, and K. Sato, High-speed 100 MHz strain monitor using fiber Bragg grating and optical filter for magnetostriction measurements under ultrahigh magnetic fields, Rev. Sci. Instrum. **88**, 083906 (2017).

[37] T. Kihara, Y. Kohama, Y. Hashimoto. S. Katsumoto, and M. Tokunaga, Adiabatic measurements of magneto-caloric effects in pulsed magnetic fields up to 55 T, Rev. Sci. Instrum. **84**, 074901 (2013).

[38] To obtain the field dependence of the CF level scheme, we used Mathematica to perform an exact diagonalization of Eq. (2) in local coordinates, utilizing CF parameters from Ref. [22]. Though Mcphase employs global coordinates for Hamiltonians, we opted not to use it for this calculation, because it would require the application of a rotation matrix, which would unnecessarily complicate the diagonalization process.

[39] M. Rotter, M. Doerr, M. Loewenhaupt, and P. Svoboda, Modeling magnetostriction in compounds using McPhase, J. Appl. Phys. **91**, 8885 (2002).

[40] M. Rotter, Using *McPhase* to calculate magnetic phase diagrams of rare earth compounds, J. Magn. Magn. Mater. **272-276**, E481 (2004).

[41] M. Rotter, M. D. Le, A. T. Boothroyd, and J. A. Blanco, Dynamical matrix diagonalization for the calculation of dispersive excitations, J. Phys.: Condens. Matter **24**, 213201 (2012).

[42] M. Rotter, A. Barcza, M. Doerr, M. D. Le, J. Brooks, E. Jobiliong, and J. Perenboom, Spin-flop transition in samarium metal investigated by capacitance dilatometry in a steady magnetic field of 45 T, Phys. Rev. B **76**, 144421 (2007).

[43] J. Jensen, Static and dynamic Jahn-Teller effects and antiferromagnetic order in PrO_2: A mean-field analysis, Phys. Rev. B **76**, 144428 (2007).

[44] T. Stöter, M. Doerr, S. Granovsky, M. Rotter, S. T. B. Goennenwein, S. Zherlitsyn, O. A. Petrenko, G. Balakrishnan, H. D. Zhou, and J. Wosnitza, Extremely slow nonequilibrium monopole dynamics in classical spin ice, Phys. Rev. B **101**, 224416 (2020).

[45] K. Baroudi, B. D. Gaulin, S. H. Lapidus, J. Gaudet, and R. J. Cava, Symmetry and light stuffing of $Ho_2Ti_2O_7$, $Er_2Ti_2O_7$, and $Yb_2Ti_2O_7$ characterized by synchrotron x-ray diffraction, Phys. Rev. B **92**, 024110 (2015).

[46] S. Kittaka, S. Nakamura, H. Kadowaki, H. Takatsu, and T. Sakakibara, Field-rotational magnetocaloric effect: A new experimental technique for accurate measurement of the anisotropic magnetic entropy, J. Phys. Soc. Jpn. **87**, 073601 (2018).

[47] G. Ehlers, A. L. Cornelius, M. Orendác, M. Kajnaková, T. Fennell, S. T. Bramwell, and J. S. Gardner, Dynamical crossover in 'hot' spin ice, J. Phys.: Condens. Matter **15**, L9 (2003).

[48] J. P. Clancy, J. P. C. Ruff, S. R. Dunsiger, Y. Zhao, H. A. Dabkowska, J. S. Gardner, Y. Qiu, J. R. D. Copley, T. Jenkins, and B. D. Gaulin, Revisiting static and dynamic spin-ice correlations in $Ho_2Ti_2O_7$ with neutron scattering, Phys. Rev. B **79**, 014408 (2009).

[49] J. A. Quilliam, L. R. Yaraskavitch, H. A. Dabkowska, B. D. Gaulin, and J. B. Kycia, Dynamics of the magnetic susceptibility deep in the Coulomb phase of the dipolar spin ice material $Ho_2Ti_2O_7$, Phys. Rev. B **83**, 094424 (2011).

[50] H. D. Zhou, C. R. Wiebe, J. A. Janik, L. Balicas, Y. J. Yo, Y. Qiu, J. R. D. Copley, and J. S. Gardner, Dynamic spin ice: $Pr_2Sn_2O_7$, Phys. Rev. Lett. **101**, 227204 (2008).

[51] Y. Machida, S. Nakatsuji, S. Onoda, T. Tayama, and T. Sakakibara, Time-reversal symmetry breaking and spontaneous Hall effect without magnetic dipole order, Nature (London) **463**, 210 (2010).

[52] K. Kimura, S. Nakatsuji, J. Wen, C. Broholm, M. Stone, E. Nishibori, and H. Sawa, Quantum fluctuations in spin-ice-like $Pr_2Zr_2O_7$, Nat. Commun. **4**, 1934 (2013).

[53] S. Petit, E. Lhotel, S. Guitteny, O. Florea, J. Robert, P. Bonville, I. Mirebeau, J. Ollivier, H. Mutka, E. Ressouche, C. Decorse, M. Ciomaga Hatnean, and G. Balakrishnan, Antiferroquadrupolar correlations in the quantum spin ice candidate $Pr_2Zr_2O_7$, Phys. Rev. B **94**, 165153 (2016).

[54] R. Sibille, N. Gauthier, H. Yan, M. Ciomaga Hatnean, J. Ollivier, B. Winn, U. Filges, G. Balakrishnan, M. Kenzelmann, N. Shannon, and T. Fennell, Experimental signatures of emergent quantum electrodynamics in $Pr_2Hf_2O_7$, Nat. Phys. **14**, 711 (2018).